precision of the radiocarbon measurements is ±4 per mil (1σ). The age model is derived from a linear interpolation procedure between the oxygen isotope results and the instrumental SST record in the Galápagos Islands by matching peaks and troughs, with an estimated error of less than 3 months. Linear trends of upwelling and nonupwelling season extremes were determined for the 1960–1975 and 1976–1983 periods and were offset by 20 per mil for the upwelling season. We did not include the 1975 upwelling nor the 1976 warm season extremes, in order to unbias the trends.
5. E. M. Druffel, *Geophys. Res. Lett.* **8**, 59 (1981).
6. J. R. Toggweiler, K. Dixon, W. S. Broecker, *J. Geophys. Res.* **96**, 50 (1991).
7. E. M. Druffel, *J. Mar. Res.* **45**, 667 (1987).
8. National Ocean Sciences Accelerator Mass Spectrometry Facility, *NOSAMS Report 94-109, WOCE AMS ^{14}C Data Report 4* (Woods Hole, MA, 1994) (courtesy of R. Key).
9. K. Wyrtki and B. Kilonsky, *J. Phys. Oceanogr.* **14**, 242 (1984); M. Tsuchiya, R. Lukas, R. A. Fine, E. Firing, E. Lindstrom, *Prog. Oceanogr.* **23**, 101 (1989); Y. Gouriou and J. Toole, *J. Geophys. Res.* **98**, 22495 (1993).
10. P. D. Quay, M. Stuiver, W. S. Broecker, *J. Mar. Res.* **41**, 769 (1983); R. M. Key *et al.*, *Radiocarbon* **38**, 425 (1996).
11. R. A. Fine, J. L. Reid, H. G. Ostlund, *J. Phys. Oceanogr.* **11**, 3 (1981); M. J. McPhaden and R. A. Fine, *ibid.* **18**, 1454 (1988); R. A. Fine, R. Lukas, F. M. Bingham, M. J. Warner, R. H. Gammon, *J. Geophys. Res.* **99**, 25063 (1994); Y. W. Watanabe, K. Harada, K. Ishikawa, *ibid.* p. 25195; M. J. Warner, J. L. Bullister, D. P. Wisegarver, R. H. Gammon, R. F. Weiss, *ibid.* **101**, 20525 (1996).
12. D. S. Luther and D. E. Harrison, *Mon. Weather Rev.* **112**, 285 (1984); A. J. Clarke and A. Lebedev, *J. Clim.* **9**, 1020 (1996); *ibid.* **10**, 1722 (1997).
13. The early shift in 1955–1956 could be the result of poor spatial coverage and instrumental bias while SST measurement techniques migrated from bucket measurements to engine intake measurements [T. P. Barnett, *Mon. Weather Rev.* **112**, 303 (1984)]. The Comprehensive Ocean-Atmosphere Data Set (COADS) database does not attempt to correct for potential instrumental biases, whereas the Global Ocean Surface Temperature Atlas (GOSTA) database does.
14. We performed a pooled *t* test of the means of the warm and upwelling seasons for the Niño-3 region using both the COADS and GOSTA databases for the periods 1956–1975 and 1976–1992. Mean upwelling SSTs are significantly different ($P < 0.01$) for both data sets. Warm season SSTs are nearly identical in the two time periods. Slight differences between data sets exist in terms of absolute SST and magnitude of change relative to the shift in 1976. However, in both data sets, mean coldest month SSTs shift 0.6° (GOSTA) to 1.0° (COADS) in relation to their post-1955 intervals.
15. S. E. Zebiak and M. A. Cane, *Mon. Weather Rev.* **115**, 2262 (1987); N. E. Graham and W. B. White, *Science* 240, 1293 (1988) and references therein.
16. We examined hydrographic profiles (2°N to 2°S, 85° to 110°W) that are archived in the Scripps Institute of Oceanography, National Oceanographic Data Center (NODC) SD2 database. Although there are not enough profiles to create seasonally resolved composite profiles, there is a consistent increase in subsurface salinity and potential temperature after 1976. The salinity increase is not enough to offset the impact of high temperatures on subsurface density. In the conductivity-temperature-depth database, the subsurface warming maxima (1.2°C) is between 40 and 80 dbar and extends to depths >300 dbar. Analysis of all available temperature data [expendable bathythermograph, mechanical bathythermograph, Integrated Global Ocean Station System (IGOSS) radio message bathythermograph, and Nansen casts archived at NODC] shows a similar profile with the subsurface temperature maximum difference of 1.6°C. The warming is persistent irrespective of the inclusion of years with strong El Niño events.
17. J. S. Vogel, J. R. Southon, D. E. Nelson, *Nucl. Instrum. Methods Phys. Res. Sect. B* **29**, 50 (1987).
18. J. C. Davis *et al.*, *ibid.* **52**, 269 (1990).
19. M. Stuiver and H. A. Polach, *Radiocarbon* **19**, 355 (1977).
20. COADS database: S. D. Woodruff, R. J. Slutz, R. L. Jenue, P. N. Steurer, *Bull. Am. Meteorol. Soc.* **68**, 521 (1987); GOSTA database: M. Bottomley, C. K. Folland, J. Hsiung, R. E. Newell, D. E. Parker, *Global Ocean Surface Temperature Atlas (GOSTA)* (U.K. Meteorological Office, Bracknell, United Kingdom, 1990); U.S. National Meteorological Center (NMC)/IGOSS database: R. W. Reynolds and T. M. Smith, *J. Clim.* **7**, 929 (1994).
21. This manuscript benefited greatly from discussions with M. Cane, G. Philander, K. Rodgers, and S. Trumbore. The authors thank M. Kashgarian, J. Southon, and E. Goddard for assistance. Critical comments and reviews were provided by E. Druffel, W. Jenkins, and two anonymous reviewers. This work was supported by a grant from NSF's program in Physical Oceanography (OCE-9796253) and by grants from the Lawrence Livermore National Laboratory (98-ERI-002 and a Center for Accelerator Mass Spectrometry minigrant). Radiocarbon analyses were performed under the auspices of the U.S. Department of Energy by the Lawrence Livermore National Laboratory (contract W-7405-Eng-48). Data will be digitally archived at the Carbon Dioxide Information Analysis Center (Oak Ridge, TN) and the World Data Center A (Boulder, CO).

30 March 1998; accepted 8 June 1998

Solidus of Earth's Deep Mantle

A. Zerr, A. Diegeler, R. Boehler

The solidus of a pyrolite-like composition, approximating that of the lower mantle, was measured up to 59 gigapascals by using CO_2 laser heating in a diamond anvil cell. The solidus temperatures are at least 700 kelvin below the melting temperatures of magnesiowüstite, which in the deep mantle has the lowest melting temperatures of the three major components—magnesiowüstite, Mg-Si-perovskite, and Ca-Si-perovskite. The solidus in the deep mantle is more than 1500 kelvin above the average present-day geotherm, but at the core-mantle boundary it is near the core temperature. Thus, partial melting of the mantle is possible at the core-mantle boundary.

The solidus of a multicomponent system relevant to that of the lower mantle plays a fundamental role for modeling the early evolution of the Earth and for understanding seismic anomalies in the D″-layer at the core-mantle boundary (CMB). Both temperature and composition of a partial melt at the solidus cannot be accurately predicted even if the melting temperatures of the end members are known. For example, it is difficult to reconcile recent findings from seismic data which suggest partial melting in the lowermost part of the mantle (*1*), with measurements in laser-heated diamond cells which have shown that the melting temperature of $(Mg,Fe)SiO_3$-perovskite, previously thought to be near the eutectic (*2*), increases rapidly with pressure (*3, 4*). The melting curve of magnesiowüstite, (Mg,Fe)O, the second most abundant lower mantle mineral, however, has a much smaller slope (*5*), and this difference in the melting behavior of the end-member components complicates the predictions of the eutectic temperature and eutectic composition in the lower mantle.

Only a few melting experiments have been done on compositions that may approximate those of the lower mantle, and these were not conducted at pressures above 25 GPa (*6, 7*). The melting temperature of olivine has been estimated at 4300 ± 270 K at about 130 GPa from a shock-wave experiment (*8*). This result provides a constraint on the binary eutectic temperature between magnesiowüstite and $(Mg,Fe)SiO_3$-perovskite. Here we describe results from measurements of the solidus temperature for a multiphase mantle-like composition over a pressure range equivalent to depths of 600 to 1500 km in the Earth (the CMB is at about 3000 km).

We used a glass approximating the composition of pyrolite (*9*) as starting material (*10*). A thin section of this glass sample with typical dimensions of 70 by 70 by <15 μm and a surface roughness of <150 nm was embedded in a diamond cell in argon, which provided inert, thermally insulating, and hydrostatic conditions. We used the CO_2-laser heating technique described elsewhere (*11*). Pressures were measured at room temperature from ruby chips located near the edge of the sample chamber. After heating, the pressure distribution throughout the pressure chamber was nearly uniform (*12*). Because of the small ratio between the volumes of the sample and pressure medium, the thermal pressure was negligible (*11*).

The quenched samples were examined by Raman spectroscopy while still at high pressure to check whether the glass had transformed to a high-pressure phase assemblage. In experiments at pressures less than 22 GPa, the spectra resembled those of β or γ-Mg_2SiO_4 plus $MgSiO_3$-majorite, the major phases of the transition zone. The Raman spectra of these high-pressure phases are unaffected by their Fe or Al contents (*13*). Of the three major lower mantle phases that would be expected to form in our

A. Zerr and R. Boehler, Max-Planck-Institut für Chemie, Postfach 3060, 55020 Mainz, Germany. A. Diegeler, Institut für Mineralogie und Geochemie der Universität zu Köln, 50674 Köln, Germany.

experiments at pressures above 24 GPa, only Mg-Si-perovskite yields a Raman signal. Ca-Si-perovskite and magnesiowüstite are Raman inactive. However, we were unable to detect any of the major Raman lines of Mg-Si-perovskite. The only indication of the presence of perovskite is a broad band near 800 cm^{-1}, which is frequently observed for $(Mg,Fe)SiO_3$-perovskites. There may be a number of reasons for the absence of the major Raman lines. Although the Raman intensities decrease with increasing pressure (*14*) and decreasing grain size, they are routinely detectable for Mg-Si-perovskites containing aluminum (*15*) or iron (*16*). Heating of samples below the solidus resulted in a grain size below 400 nm, which is evident from the atomic-force microscope (AFM) analysis, but we suspect that perovskite containing aluminum, iron, and other transition metals may possess higher symmetry, thus lowering the Raman activity. We were unable to determine the chemical composition of individual grains in our fine-grained aggregates by classical analytical methods. However, we were able to check for chemical zoning due to Soret diffusion, crystallization, or melting on a larger scale by using raster mode element mapping with an electron microprobe. Below the solidus, we observed a uniform distribution of Si, Mg, Al, Ca, and Fe throughout the entire sample. Above the solidus, the melted region showed slight depletion in Ca and Fe for all our experiments, but this result may be biased by topographical effects (see below), which were clearly observed for the lighter elements Mg and Si.

In our previous melting experiments on the individual lower mantle phases (*3, 5, 17*), melting was evidenced by changes in the absorption of CO_2 laser radiation. However, there was no such signal in this series of experiments, probably because of the modest amount of melt produced at the solidus. For this reason, we instead determined the onset of melting by monitoring textural changes on the quenched samples under the optical microscope while they were still under pressure and on the recovered samples by using an AFM and a scanning electron microscope (SEM) (*18*). To determine the solidus temperature, we held a sample at some pressure and temperature conditions for at least 5 min. Temperature fluctuations were carefully avoided by using a temperature stabilization technique (*11*). After quenching, the sample was optically examined under the microscope while it was still under pressure. In the experiments, temperatures were increased in steps of about 200 K until melt features (see below) were observed optically in the quenched samples. The melted sample was then examined by AFM and SEM, because optical examination of very small features can be unreliable. If melt features were verified, a new sample was taken to about the same pressure, but held at 200 K below the previous temperature, and examined under the AFM and the SEM. In this way, the upper and the lower bounds for the solidus were established.

Backscattered electron images (*18*) of two samples heated at 23.7 ± 0.3 GPa and 20.6 ± 0.4 GPa, respectively, are shown (Fig. 1). The first sample, heated to 2310 ± 90 K, shows a smooth surface. The cracks, which became evident after pressure was released, are due to stresses associated with crystallization of the high-pressure phases and are not present in the surrounding glassy portion of the sample where temperatures were too low for crystallization. The second sample also shows cracks in the crystalline portion, but there are also new textural features of a different type in the center of the hot spot that reached 2550 ± 30 K (Fig. 1B, arrow). From quantitative topographic measurements with an AFM (Fig. 2), we interpret these features as molten material that migrated in the molten argon pressure medium (*19*) to-

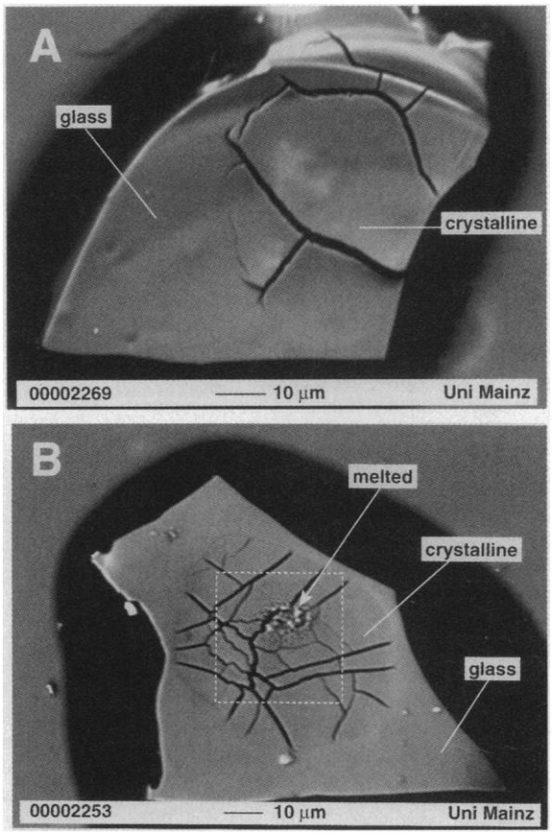

Fig. 1. Evidence of the first appearance of melt for a pyrolite-like composition from back-scattering electron topographic images. The glass sample was heated with a defocused laser beam, producing small radial temperature gradients (*24*) and leaving the outer portion of the sample below the critical crystallization temperature. Within a circular patch of about 50 μm in diameter, the starting material has converted to a crystalline high-pressure phase assemblage. Cracks within this portion became evident after pressure release. (**A**) The highest temperature in the center of the hot spot was 2310 K, just below the solidus at 23.7 GPa. (**B**) Sample heated just above the solidus to 2550 K at 20.6 GPa exhibits features similar to those in (A). In addition, new textural features (about 10 μm in diameter) appeared as a result of melting and migration of molten material toward the laser beam, which is evident from quantitative topographic measurements in the area indicated by dashed lines (Fig. 2).

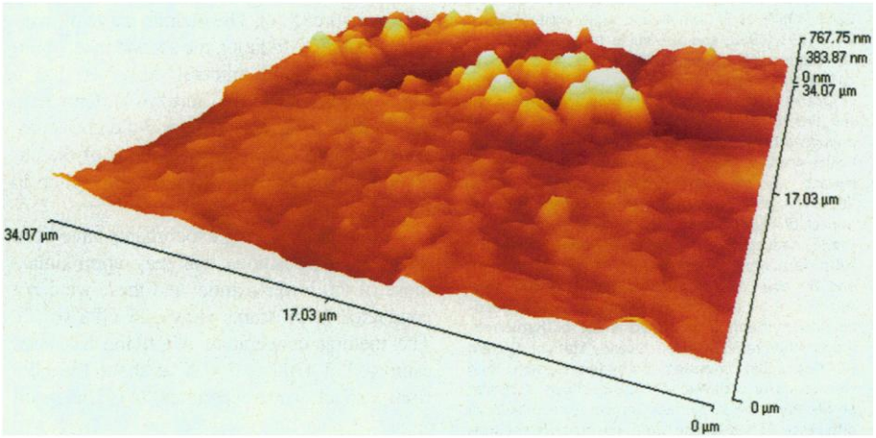

Fig. 2. Three-dimensional surface topography of the 34 μm by 34 μm area shown in Fig. 1B measured with an AFM. The sample melted within an area of about 10 μm in diameter and migrated toward the laser beam, causing height variations of up to 0.77 μm. In contrast, height variations in the surrounding subsolidus material area are smaller than 0.2 μm.

ward the laser beam. Migration of molten material in liquid pressure media toward the laser beam was also observed in melting experiments for cubic BN (*20*), MgO, $(Mg,Fe)SiO_3$-perovskite, and $CaSiO_3$-perovskite.

Our results to 59 GPa are shown (Fig. 3). Only the highest subsolidus and the lowest temperatures at which melting was observed are shown. These data bracket the solidus to within about 300 K, similar to multianvil experiments near 20 GPa. At transition zone pressures, our data agree with multianvil determinations of the mantle solidus (*6, 7, 21*).

Our measured pyrolite solidus lies approximately parallel to the melting curve of magnesiowüstite (*5*), but it is offset to lower temperatures by about 700 K (Fig. 4). The similarity of the melting slopes of magnesiowüstite and pyrolite is plausible. Because the melting slope of magnesiowüstite with respect to the two perovskites (*17*) is relatively low, the eutectic composition should shift toward (Mg,Fe)O with increasing pressure (*2*). For extrapolation we have assumed that this similarity is maintained at higher pressures and extended the solidus parallel to the melting curve of magnesiowüstite, which follows a Lindemann melting law, and obtained a solidus temperature at the CMB (135 GPa) of about 4300 K. The assumption that the solidus of a pyrolite composition is dominated by the melting behavior of magnesiowüstite is supported by the agreement of our data with eutectic temperatures measured in a $MgSiO_3$-$(Mg_{0.85},Fe_{0.15})O$ assemblage (*17*). In addition, the extrapolation is in good agreement with the shock melting point of 4300 ± 270 K at 130 GPa (*8*) for olivine, which breaks down into a perovskite-magnesiowüstite assemblage during shock.

Our solidus temperatures are about 1300 K above an average lower mantle adiabat (*22*) at midmantle pressures, and the extrapolated solidus temperature of about 4300 K is just above that of the outer core at the CMB, as deduced from melting temperature measurements on the Fe-O-S system (4000 ± 200 K) (*23*).Thus, partial melting of normal mantle material in close proximity to the core is indeed plausible.

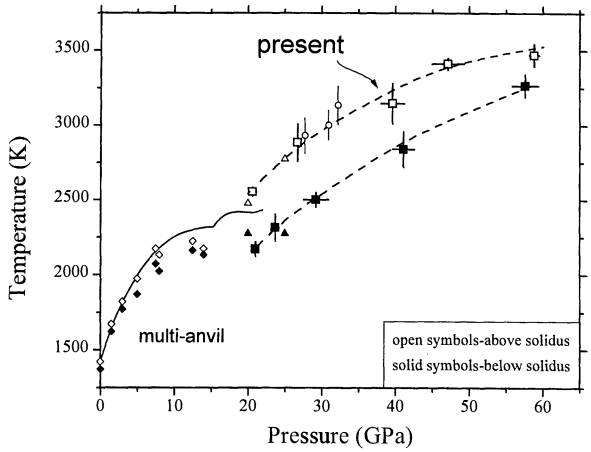

Fig. 3. Solidus of mantle relevant materials. Both current data above 20 GPa (squares), connected by dashed curves, and previous multianvil work for peridotites [diamonds for KLB-1 (*21*), triangles for PHN-1611 (*6*)], have upper (open symbols) and lower bounds (solid symbols) for the solidus. Solid line is an average estimate of the solidus for KLB-1 peridotite (*7*). Open squares represent the appearance of first melt; solid squares are the last subsolidus points. Temperature error bars represent temperature fluctuations during heating. Pressure error bars include the pressure variation in the sample chamber and the uncertainty in thermal pressure. Open circles show eutectic temperatures of a $MgSiO_3$-$(Mg_{0.85},Fe_{0.15})O$ assemblage measured in a diamond cell with an Nd-yttrium-lithium-fluoride laser (*17*).

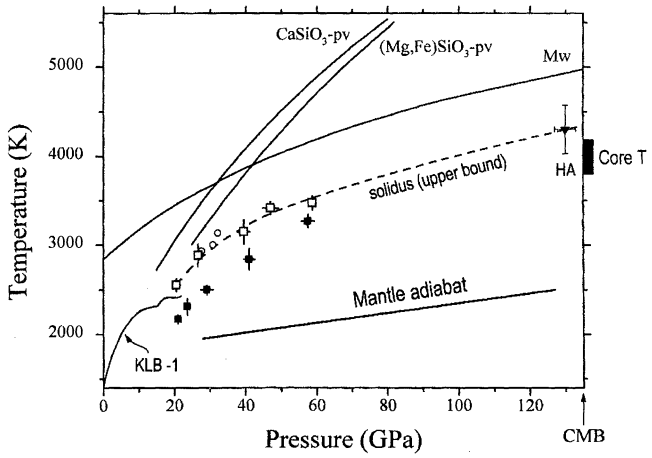

Fig. 4. Upper bound of the solidus (dashed line) extrapolated to the CMB, assuming a slope similar to that of $(Mg_{0.85},Fe_{0.15})O$-magnesiowüstite (*5*). Experimental data use the same symbols as in Fig. 3. Melting temperatures of the major lower mantle phases magnesiowüstite $(Mg_{0.85},Fe_{0.15})O$ (Mw), $(Mg,Fe)SiO_3$-perovskite (pv) and $CaSiO_3$ perovskite (solid lines) are from Zerr *et al.* (*3, 5, 17*) and the solidus for the peridotite KLB-1 is from Zhang and Herzberg (*7*). The shock melting point of olivine (HA) (*8*) is in agreement with the current extrapolation. The average lower mantle temperature profile is represented by an adiabat calculated from seismic data (*22*), and the core's temperature at the CMB was obtained from melting temperature measurements in the Fe-O-S system (*23*).

References and Notes

1. L. Wen and D. V. Helmberger, *Science* **279**, 1701 (1998); Q. Williams and E. J. Garnero, *ibid.* **273**, 1528 (1996).
2. E. Ito and T. Katsura, in *High Pressure Research: Application to Earth and Planetary Sciences*, Y. Syono and M. H. Manghnani, Eds. (Terra, Tokyo, 1992), pp. 315–322.
3. A. Zerr and R. Boehler, *Science* **262**, 553 (1993).
4. G. Shen and P. Lazor, *J. Geophys. Res.* **100**, 17699 (1995).
5. A. Zerr and R. Boehler, *Nature* **371**, 506 (1994).
6. E. Ito and E. Takahashi, *ibid.* **328**, 514 (1987).
7. J. Zhang and C. Herzberg, *J. Geophys. Res.* **99**, 17729 (1994).
8. K. G. Holland and T. J. Ahrens, *Science* **275**, 1623 (1997).
9. A. E. Ringwood, *Composition and Petrology of the Earth's Mantle* (McGraw-Hill, New York, 1975); W. F. McDonough and S.-s. Sun, *Chem. Geol.* **120**, 223 (1995).
10. A glass sample was used because it is chemically more homogeneous than a mixture of oxides and silicates on the small scale in the diamond cell, thus providing uniform laser heating. The sample was synthesized by A. Borisov (Institut für Mineralogie und Geochemie der Universität zu Köln) from nine oxides (listed below) in pyrolite proportions. The mixture was molten in a platinum wire loop in a reducing atmosphere (CO/CO_2, 5:2) at 1930 K. Optical and Raman spectroscopic analysis of the quenched glass droplet showed small amounts of crystalline olivine (10 to 30 μm). Microprobe analysis of the glass with a JEOL (JXA 8900 RL, University of Mainz), yielded the following composition (in weight %): SiO_2, 49.1; TiO_2, 0.3; Al_2O_3, 4.6; Cr_2O_3, 0.5; FeO, 6.2; NiO, 0.03; MgO, 35.7; CaO, 3.5; Na_2O, 0.1. This differs from Ringwood's pyrolite in having MgO/(MgO + FeO) = 0.91 rather than 0.89, and it is substantially higher in SiO_2.
11. R. Boehler and A. Chopelas, *Geophys. Res. Lett.* **18**, 1147 (1991). A power-stabilized 150-W CO_2 laser (90% TEM00) was used for heating. The small sample thickness and the effective thermal insulation of the sample from the diamond by the argon pressure medium allowed defocusing of the laser beam to reach high temperatures with small axial and radial gradients. Large portions of the samples were thus converted to high-pressure minerals from the glass starting material without scanning the laser beam. Thermal radiation spectra were recorded from areas 2 to 3 μm in diameter with a charge-coupled device detector in the wavelength range 500 to 815 nm, and Planck's radiation function was fitted to the spectra. The emissivity of the sample was taken to be independent of wavelength. The temperature uncertainty based on this assumption is about ±150 K (*2*). The temperatures reported in this work are maximum temperatures in the center of the laser-heated spot.
12. G. Serghiou, A. Zerr, L. Chudinovskikh, R. Boehler, *Geophys. Res. Lett.* **22**, 441 (1995).
13. P. McMillan *et al.*, *Phys. Chem. Min.* **16**, 428 (1989); P. McMillan and M. Akaogi, *Am. Mineral.* **72**, 361 (1987).
14. A. Chopelas and R. Boehler, in *High Pressure Research: Application to Earth and Planetary Science*, Y. Syono and M. Manghnani, Eds. (Terra, Tokyo, 1992), pp. 101–108.
15. G. Serghiou, A. Zerr, A. Chopelas, R. Boehler, *Phys. Chem. Minerals* **25**, 193 (1998).
16. G. Serghiou, A. Zerr, R. Boehler, *Science* **280**, 2093 (1998).
17. A. Zerr, G. Serghiou, R. Boehler, *Geophys. Res. Lett.* **24**, 909 (1997).
18. Backscattering electron (topographic) images were made with the SEM unit of JEOL JXA 8900 RL. For quantitative measurements of the sample topography, we used an AFM (Explorer, Topo Metrix) operated in the contact mode [R. Wiesendanger and H.-J. Güntherodt, Eds., *Scanning Tunneling Spectroscopy II and III; Springer Series in Surface Sciences* (Springer-Verlag, Berlin, ed. 2, 1995 and 1996)], vols. 28 and 29.
19. C.-S. Zha, R. Boehler, D. A. Young, M. Ross, *J. Chem. Phys.* **85**, 1034 (1986).

20. A. Zerr, G. Serghiou, R. Boehler, *Proceedings of the Fifth NIRIM International Symposium on Advanced Materials*, Tsukuba, Japan, 1 to 5 March 1998 (National Institute for Research in Inorganic Materials, Tsukuba, Japan, 1998), pp. 5–8.
21. E. Takahashi, *J. Geophys. Res.* **91**, 9367 (1986).
22. J. M. Brown and T. S. Shankland, *Geophys. J. R. Astron. Soc.* **66**, 579 (1981).
23. R. Boehler, *Annu. Rev. Earth Planet. Sci.* **24**, 15 (1996).
24. R. Boehler, *Philos. Trans. R. Soc. London Ser. A* **354**, 1265 (1996).
25. We thank V. Hillgren, B. Schulz-Dobrick, and G. Serghiou for helpful discussions and V. Hillgren, G. Serghiou, and the reviewers for constructive comments on the manuscript.

2 March 1998; accepted 18 May 1998

A Reduction-Pyrolysis-Catalysis Synthesis of Diamond

Yadong Li,* Yitai Qian,* Hongwei Liao, Yi Ding, Li Yang, Cunyi Xu, Fangqing Li, Guien Zhou

Diamond powder was synthesized through a metallic reduction-pyrolysis-catalysis route with the reaction of carbon tetrachloride and sodium at 700°C, in which the sodium was used as reductant and flux. This temperature is much lower than that of traditional methods. The x-ray powder diffraction patterns showed three strong peaks of diamond. The Raman spectrum showed a sharp peak at 1332 inverse centimeters, which is characteristic of diamond. Although the yield was only 2 percent, this method is a simple means of forming diamond.

The properties of diamond materials, such as optical properties, high hardness, high thermal conductivity (*1*), and semiconductivity induced by doping, have led to considerable efforts to create diamond since the first report of diamonds synthesized through a high-pressure high-temperature process (*2*). Diamonds made with the TNT detonation method were composed of nanometer-sized spherical particles (*3, 4*). Micrometer-sized diamonds have been grown in a hydrothermal process using carbon, water, and metal near 800°C and at 1.4 kbar pressure, but diamond seeds were needed (*5, 6*). Chemical vapor deposition (CVD) (*7–10*) is a low-pressure synthetic route to the synthesis of polycrystalline diamond films, which uses CH_4 or C_2H_2 as a carbon source. Through the action of thermal filament–assisted CVD, plasma CVD, or combustion flame CVD, the carbon source decomposed to form active carbon (in the sp^3 hybrid state), which formed diamondlike structure films. In traditional organic synthesis, the Wurtz reaction (*11*) $R^1X + R^2X + 2Na \rightarrow R^1\text{–}R^2 + 2NaX$ can be used to form carbon-carbon bonds between alkyl groups. If CCl_4 is treated with Na under appropriate temperature and pressure, the carbon atoms could connect to form a three-dimensional network; such a network based on the sp^3 hybrid state could be diamond. Here, we selected CCl_4 as a carbon source to synthesize diamond by using Na as reductant and flux at 700°C in the presence of a metal catalyst (*2, 12*). Diamond was formed, although at a low yield (~2%). The process could be proposed as

$$CCl_4 + 4Na \xrightarrow[\text{Ni–Co}]{700°C} C(\text{diamond}) + 4NaCl \qquad (1)$$

We call it the reduction-pyrolysis-catalysis (RPC) route. According to the free energy calculations $\Delta G°$ (diamond) = −416.7 kcal mol^{-1} and $\Delta G°$ (graphite) = −417.4 kcal mol^{-1}, $CCl_4 + 4Na \rightarrow C(\text{diamond}) + 4NaCl$ and $CCl_4 + 4Na \rightarrow C(\text{graphite}) + 4NaCl$ are thermodynamically spontaneous. Formation of graphite (amorphous carbon) and diamond is possible, and the yield of graphite (amorphous carbon) and diamond may be determined by kinetics. X-ray powder diffraction (XRD) patterns showed three strong peaks of diamond [(111), (220), and (311)] and gave a lattice constant of 3.569 Å, which is near the reported value (*13*). The Raman spectrum showed a sharp peak at 1332 cm^{-1}, which represented diamond (*14*).

An appropriate amount of CCl_4 (5 ml) and an excess of metal Na (20 g) were put into a stainless steel autoclave of 50-ml capacity, and then several pieces of Ni-Co alloy (Ni:Mn:Co, 70:25:5 by weight) were added to the autoclave as a catalyst. The autoclave was maintained at 700°C for 48 hours and then allowed to cool to room temperature. At the beginning of the reduction, there was high pressure in the autoclave. However, as CCl_4 was reduced by metal Na, the pressure in the autoclave decreased. The products were washed with absolute ethanol, then with 6 mol $liter^{-1}$ HCl, and then with distilled water. The final powder was dried in an oven. A grayish-black powder was obtained with a density of 3.21 g cm^{-3}. This value is less than face-centered cubic diamond (3.51 g cm^{-3}) and may be due to the presence of a coating of amorphous carbon on the diamond.

The XRD pattern was recorded on a Rigaku D/max rA x-ray diffractometer with Cu Kα radiation [wavelength (λ) = 1.54178 Å]. The XRD patterns (Fig. 1) show three strong peaks of diamond [(111), (220), and (311)] and these patterns can be indexed to the cubic cell of diamond with a lattice constant a = 3.569 Å, which is near the reported values (*13*). However, in the pattern, there is a stronger wide peak at ~26° (2θ), indicating a significant amount of amorphous carbon; and there are also weaker peaks, indicating the existence of a catalyst alloy after the product was washed with acid. These weaker peaks may appear because the alloy particles were coated by carbon and were

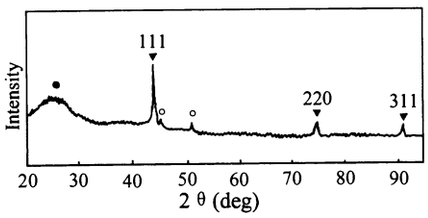

Fig. 1. X-ray diffraction pattern of sample. Diamond peaks, ▼; amorphous carbon, ●; Ni-Co alloy peaks, ○.

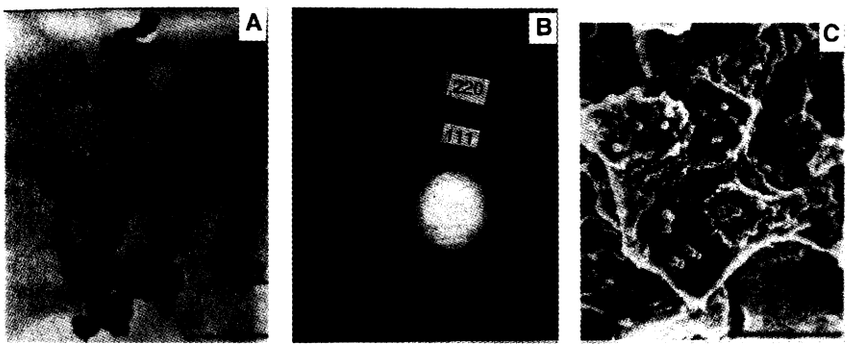

Fig. 2. (**A**) Transmission electron microscopy image of sample (scale bar, 1 μm), (**B**) electron diffraction pattern, and (**C**) SEM image (scale bar, 60 μm).

Structure Research Laboratory and Department of Chemistry, University of Science and Technology of China, Hefei, Anhui 230026, People's Republic of China.

*To whom correspondence should be addressed.